# Investigation of longitudinal friction characteristics of an omnidirectional wheel via LuGre model

Osman Nuri Şahin*⊙ and Mehmet İsmet Can Dede

*Department of Mechanical Engineering, Izmir Institute of Technology, Izmir, Turkey*

## SUMMARY
In recent years, omnidirectional wheels have found more applications in the design of automated guided vehicles (AGV). In this work, LuGre friction model is used for an omnidirectional wheel. A test setup that includes a single omnidirectional wheel is designed and constructed to identify the model parameters. With the help of the constructed test setup, the longitudinal friction characteristic of the omnidirectional wheel is obtained, and the model is verified via validation tests. In addition, for the first time, the effect of lateral frictional force on longitudinal motion is examined for an omnidirectional wheel through experiments.

KEYWORDS: Holonomic mobile robot; Wheel friction model; Omnidirectional wheels; Wheel slippage.

## 1. Introduction
Automated guided vehicles (AGVs) are used in various working areas such as factories, households and even on a planet's surface. Consequently, they have locomotion systems that are tailored to their working environments. Although there are various locomotion systems, such as legs and pallets, for the motion of terrestrial mobile robots, wheels are the most commonly employed locomotion system. Wheels used in wheeled mobile robots (WMRs) vary in terms of their design and material types. Although in the literature there are wheels specially designed for the purpose of increasing the mobility of a mobile robot or to enable more convenient motions in the working area[1–4] many wheels used in mobile robots are actually wheels designed for different purposes.[5–7] Nevertheless, there is no standard friction model that is applied for these different types of wheels.

The friction characteristic of the wheel is an important factor affecting the motion ability of WMRs. Having knowledge about this characteristic is helpful for improving the control of mobile robots[8] when absolute position measurements for localization are not available. In fact, for the localization of mobile robots working in indoor applications, such as AGVs and household robots, global positioning systems (GPS) are not available. Instead, sensor fusion that combines odometry data taken from wheel's angular speed sensor (commonly an encoder or a tachometer) and other sensors like inertial measurement units (IMU) or laser sensors are more suitable for indoor robot-positioning tasks.[9–12] The difficulty of positioning with odometry data is that because of wheel slippage, the actual position of the robot cannot be calculated precisely. Therefore, the estimation of wheel slippage with the help of frictional force models becomes an important topic in improving robot positioning with odometry data.[13]

Wheels used in mobile robot applications are quite different than the tires used in automobiles. Although in the literature there are various studies that describe friction characteristics of automobile tires,[14–18] there are few studies that deal with modeling mobile robot wheel friction with static and
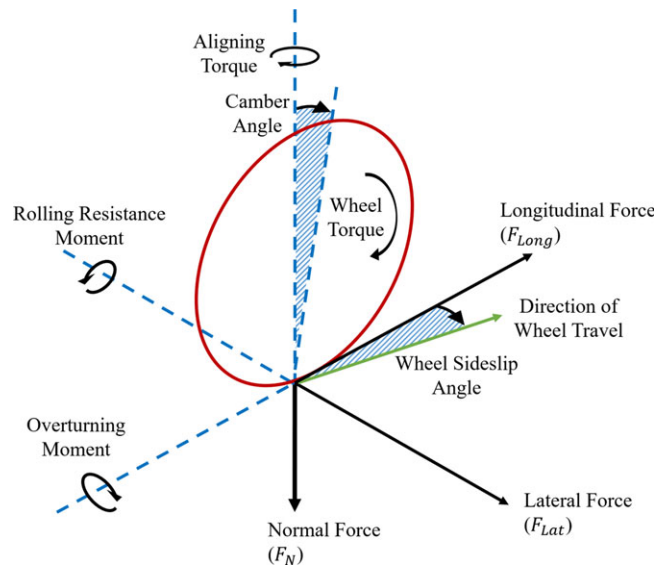
*Corresponding author. E-mail: osmansahin@iyte.edu.tr

Fig. 1. Forces and moments acting on the wheels.[21]

kinetic friction coefficients[19,20] or steady-state friction model.[8] Achieving traction control of the mobile robot and improving localization with odometry data require information on wheel's friction characteristics. Therefore, these characteristics must be revealed before these kinds of studies can be carried out with an actual mobile robot.

WMRs need motion ability that allows them to move over rocks or holes and avoid obstacles in outdoor operations. In contrast to outdoor environments, indoor environments have relatively smooth and clean surfaces. However, there are many obstacles and narrow passages in indoor tasks that require increased mobility capabilities. Among the tasks that require maneuvering in tight spaces and avoiding obstacles, the following can be named as examples: transporting of goods in hospitals or factories, public area cleaning and sheltered workshops for disabled people. Consequently, special omnidirectional wheels have been developed in the past years to increase the mobility capabilities of WMRs. Using these types of wheels, WMRs can be developed with holonomic motion ability. Holonomic mobile robots (HMRs) are capable of translating in two orthogonal directions and rotating about the normal of the surface independently and simultaneously.

Motion of wheeled vehicles is accomplished by forces that are transmitted to the ground via wheels. Commonly in conventional car-like vehicle models, three forces – lateral force ($F_{Lat}$), which is parallel to the rotation axis of the wheel, longitudinal force ($F_{Long}$), which is perpendicular to the rotation axis, and normal force ($F_N$), which is perpendicular to the surface – and three moments acting at the contact area between the tire and the ground are used, as denoted in Fig. 1. Unlike car-like vehicles' tires, the contact between the universal type omnidirectional (UTO) wheel and the ground can be modeled as a point type of contact. Therefore, the aligning torque is in negligible range. Also, rolling resistance can be neglected for stone-like hard materials, but if floor material is soft and deformable by UTO wheel, rolling resistance should be considered. On the other hand, while the UTO wheel rolls at some instances, there are two contact points since the UTO wheel has two rows of rollers (Figs 6(b) and 7) Consequently, the overturning moment cannot be neglected. Although the lateral force acting on the wheel is considerably small since there are passive roles that allow lateral motion of the UTO wheel, this force might change the longitudinal frictional force effects on the wheel. Therefore, longitudinal wheel friction models and effect of the lateral frictional force of the omnidirectional wheel on longitudinal motion are considered in this study.

Longitudinal force is a function of normal force and normalized friction coefficient of the wheel as presented in Eq. (1).

$$F_{Long} = \mu F_N \tag{1}$$

Longitudinal slip ratio ($s$) is a ratio between the absolute speed of the vehicle ($V$) and the speed of the vehicle calculated using the wheel's angular speed ($r\omega$). Here, $\omega$ is the angular speed and $r$ is
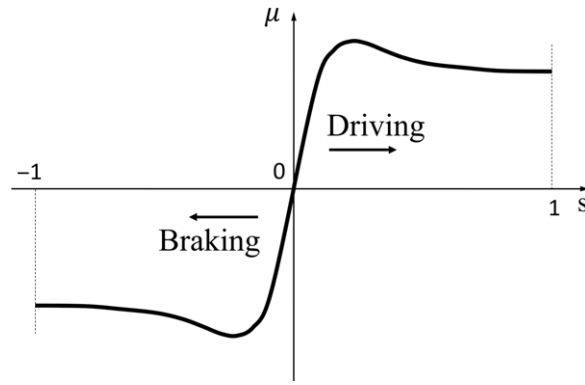
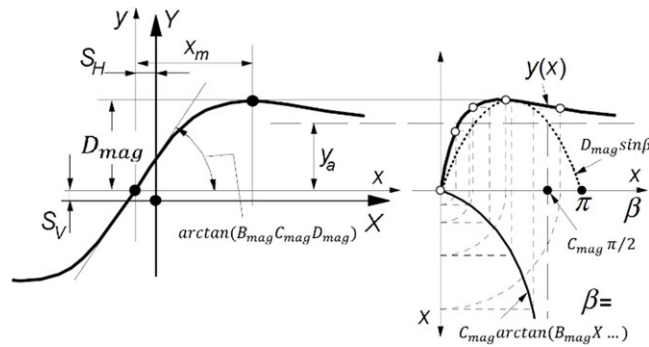Fig. 2. Tire friction coefficient characteristic curve.[22]



Fig. 3. Magic formula parameters to produce steady-state wheel friction curve.[23]

the radius of the wheel. In a steady-state case, there is a nonlinear relation between the normalized friction coefficient ($\mu$) and the longitudinal slip ratio as represented in Fig. 2. The longitudinal slip ratio varies depending on the brake and driving situation as presented below.

$$s = \begin{cases} s_b = \dfrac{r\omega}{v} - 1 & \text{if} \quad v > r\omega, \, v \neq 0 \text{ for braking} \\ s_d = 1 - \dfrac{v}{r\omega} & \text{if} \quad v < r\omega, \, \omega \neq 0 \text{ for driving} \end{cases} \tag{2}$$

In the literature, there are some semi-empirical models that represent steady-state behaviors of the wheel friction. The most commonly used semi-empirical wheel friction model is Pacejka's model, which is called "Magic Formula."[23] Steady-state force and moment characteristics of the wheel are described by a number of parameters in this "Magic Formula" given below:

$$Y = D_{mag} sin \left[ C_{mag} \arctan \left\{ B_{mag} X - E_{mag} \left( B_{mag} X - \arctan B_{mag} X \right) \right\} \right] \tag{3}$$

where $B_{mag}$ is stiffness factor, $C_{mag}$ is shape factor, $D_{mag}$ is peak value and $E_{mag}$ is curvature factor. The meaning of the parameters of the magic formula to produce a curve that fit experimental data is represented in Fig. 3. Steady-state behaviors of the wheel for different road conditions can be modeled by adjusting these parameters.

These kinds of models do not represent the transient behavior of the wheel. In fact, friction characteristic models are investigated based on two types of models: static friction and dynamic friction models. Static friction models are used for studying steady-state behaviors of the wheel friction. These models define the wheel friction characteristics when the linear speed of the vehicle and angular speed of the wheel are constant. Dynamic wheel friction models are used to model both transient and steady-state behaviors of the wheel friction. A major difference of dynamic models with respect to static friction models is that dynamic models are useful for modeling the behaviors of the wheel when the vehicle accelerates or decelerates. Hence, dynamic wheel friction models should be able to represent both steady-state and transient behaviors of the wheel.[24] Dynamic models for longitudinal

wheel friction are separated from each other according to the contact definition between the wheel and the ground:

(1) Lumped models assume point type of contact with the ground;
(2) Distributed models assume the contact patch is an area.

Distributed wheel friction models are more realistic but relatively more complex with respect to lumped models. In reality, all wheels have a force distribution area. Nevertheless, since this area is relatively smaller for solid wheels that are made by rubber-like materials, the point type of contact is used in the model for these kinds of wheels. Distributed models are more suitable in modeling the friction of conventional car-like vehicles' tires that have pressurized air inside. In UTO wheels, located at the outer circle of the wheel, there are passive rollers that are produced by a solid material. Consequently, the contact area of a UTO wheel is very small. Therefore, lumped friction models are more appropriate for modeling these wheels.

The main contribution of this study is the development of a friction model of the UTO wheel that is used in indoor mobile robot applications. This model considers the effect of the lateral frictional force on the longitudinal motion for the first time in the literature.

In the next section, the methodology is explained in terms of the friction model to be exploited, and the construction of the test setup for the estimation of this friction model's parameters is presented. Additionally, the dynamic equations of motion of the test setup and the construction properties are described. In the fourth section, parameter estimation methods used in this study are given, and the identification and system model validation test results are presented. Also, the test results that represent the effect of the lateral frictional force of the UTO wheel on longitudinal motion of a mobile robot are presented in the last section. This article concludes by discussing the obtained results.

## 2. Methodology
In this section, the selected approach to model the friction of UTO wheels is described, and then the test setup used for the identification of this model's parameters is explained. The test setup is a quarter model of a WMR that has UTO wheels. The dynamic equations of this quarter model are derived to facilitate the comprehension of the devised methodology.

One of the lumped friction models for representing the longitudinal wheel friction is Clover's longitudinal wheel friction model. This model is based on the relation between the speed of the wheel and the deformation of a virtual brush that is deformed by the longitudinal force at a hypothetical point at the contact patch of the wheel.[25] Another model is the Dahl model (otherwise known as solid friction model), which is designed for modeling friction in simulations of dynamic systems.[26] This model represents friction characteristics in terms of the strength properties of solid materials. According to the Dahl model, static friction and Coulomb friction characteristics resemble ultimate and rupture stresses that are defined in stress–strain diagrams. Canudas et al. proposed the LuGre model that is an extension of the Dahl model by including the Stribeck friction effect.[27] In order to receive similar results for both actual steady-state and transient friction characteristic of a wheel, the LuGre model used to model the longitudinal friction characteristics of the UTO wheel in this study is represented as follows:

$$\dot{p} = V_r - \frac{\sigma_0 \, |V_r|}{g(V_r)} p \tag{4}$$

$$F = (\sigma_0 p + \sigma_1 \dot{p} + \sigma_2 V_r) F_N \tag{5}$$

$$g(V_r) = \mu_c (\mu_s - \mu_c) \, e^{-|V_r/V_s|^{1/2}} \tag{6}$$

where $V_r$ is the relative speed; $\sigma_0$ and $\sigma_1$ are longitudinal lumped stiffness and damping of the wheel, respectively; $\sigma_2$ is viscous relative damping, $\mu_c$ and $\mu_s$ are normalized Coulomb and viscous friction coefficients, respectively; $p$ is internal relative state; $V_s$ is Stribeck relative speed; and $F_N$ is normal force acting on the wheel.

The LuGre model parameters should be estimated to model longitudinal wheel friction between the UTO wheel and the floor material of the robot's workspace. An experimental test setup that contains one-quarter of a four-UTO-wheeled HMR is designed and built for this purpose.
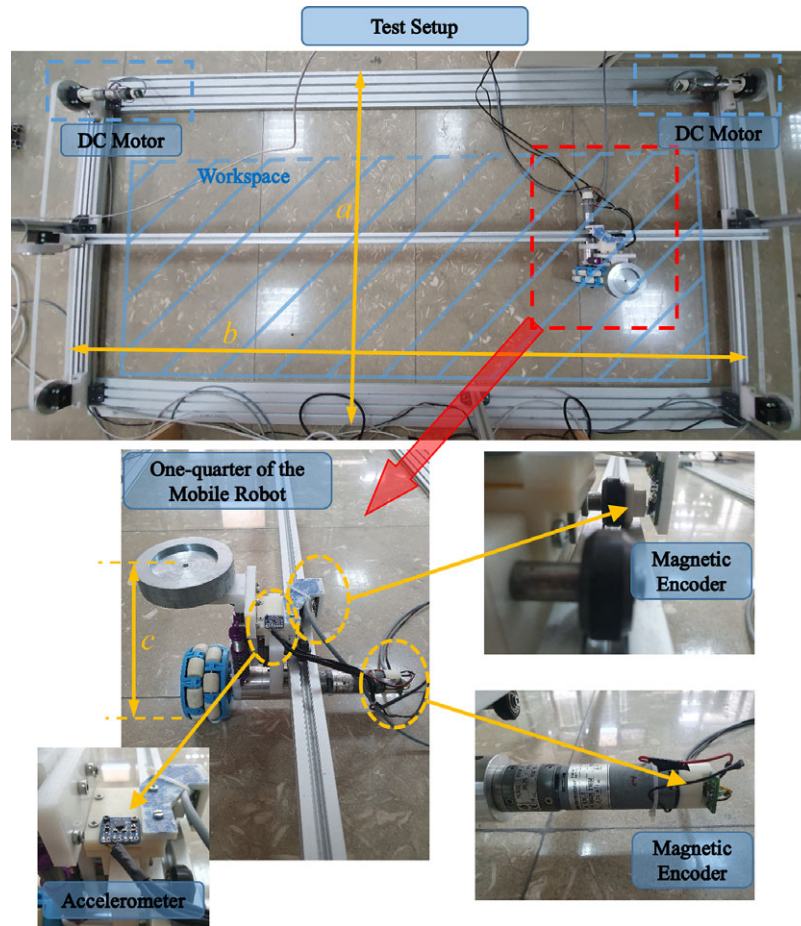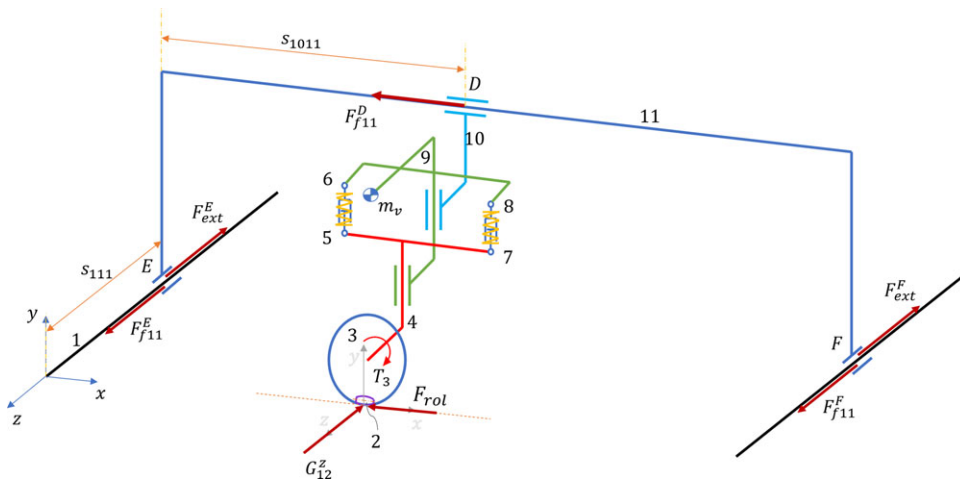
Fig. 4. Experimental test setup.



Fig. 5. Schematic representation of the test setup.

## 2.1. Experimental test setup

The experimental test setup shown in Fig. 4 includes one-quarter of an HMR with a single UTO wheel. This one-quarter part of the mobile robot includes links 2–9 that are represented in the schematics of the test setup presented in Fig. 5. The one-quarter part is mounted on a linear rail on the bridge that is constructed with aluminum sigma profile (link 11). The linear rail is composed of two small wheels rolling on the aluminum sigma profile; hence the prismatic joint structure is not

shape-closed. This makes the tilt of the vehicle free, and the effects of the overturning moment are observable in this test setup. This bridge is responsible for both balancing the one-quarter part and guiding the motion of the part along the direction that is perpendicular to the rotation axis of the UTO wheel. The bridge is mounted on two rails, which are located on the ground, at points $E$ and $F$ with two prismatic joints. Motion on these two rails provides translation of the bridge and the one-quarter part along the axis that is parallel to the rotation axis of the wheel. The dimensions of the test setup are $a = 1000$ mm, $b = 2100$ mm and $c = 250$ mm. The workspace of the one-quarter part inside of the test setup is $600 \times 1700$ mm.

One of three DC motors used in this setup is coupled to the shaft of the UTO wheel, and the other two are connected to belt-pulley systems that are responsible for the linear motion of the wheel in two translational axes of the surface. All DC motors used in the test setup are Dunkermotoren$^{\text{TM}}$ brand G30.0 model with gearboxes that have a 20.25:1 gear ratio. These motors are driven with three Maxon$^{\text{TM}}$ ADS 50/10 4-Q-DC Servo amplifiers. The motor mounted on the UTO wheel is driven in current mode in order to obtain actuation torque and traction force relation. Humusoft$^{\text{TM}}$ MF624 model data acquisition card is used to collect data from the various sensors and to provide input to the servo amplifiers.

In order to estimate the wheel traction force with the LuGre model, relative speed – which is the difference between the speed of the vehicle calculated using the wheel speed ($\dot{\theta}_3$) and the absolute speed of the vehicle ($\dot{s}_{1011}$) – should be known. The wheel speed and the linear guide speed are measured separately with magnetic encoders. The acceleration of the vehicle is measured by an analog accelerometer. The total mass of the one-quarter part is adjusted with additional mass ($m_v$) to represent a quarter of the HMR mass.

### 2.2. Dynamic equations of the test setup

In order to derive dynamic equations of motion for the test setup, Lagrange's method is implemented. The dynamics along the $Y$-axis is neglected as it does not affect the longitudinal dynamics of the wheel on the horizontal plane. The general Lagrange equation is represented as

$$\frac{\partial}{\partial t}\left(\frac{\partial L}{\partial \dot{q}}\right) - \frac{\partial L}{\partial q} + \frac{\partial D_{dis}}{\partial \dot{q}} = Q_K \tag{7}$$

where $L$ is the Lagrange function, $q$ is the column vector of generalized coordinates, $D_{dis}$ is dissipation function and $Q_K$ is $k$th generalized force. For test setup, generalized coordinates are identified as

$$q = \begin{bmatrix} s_{111} \\ \theta_3 \end{bmatrix} \tag{8}$$

Since the potential energy change can be assumed to be zero, the Lagrange function of the system is composed by the kinetic energy functions as follows:

$$L = \frac{1}{2}m_T V_T^2 + \frac{1}{2}m_{11} V_{11}^2 + \frac{1}{2}I_3 \omega_3^2 \tag{9}$$

where $V_T$ is the speed of the total mass ($m_T$) of links 2–10 and attached additional mass ($m_v$) in order to simulate the mass of the mobile robot, $m_{11}$ is the mass of link 11, $V_{11}$ is the speed of link 11, $I_3$ is the moment of inertia of link 3, which is the UTO wheel, calculated about the UTO wheel's rotation axis, and $\omega_3$ is the angular speed of link 3.

$$m_T = \sum_{i=2}^{10} m_i + m_v \tag{10}$$

$$\omega_3 = \dot{\theta}_3 \tag{11}$$

$$V_T^2 = \dot{s}_{1011}^2 + \dot{s}_{111}^2 \tag{12}$$
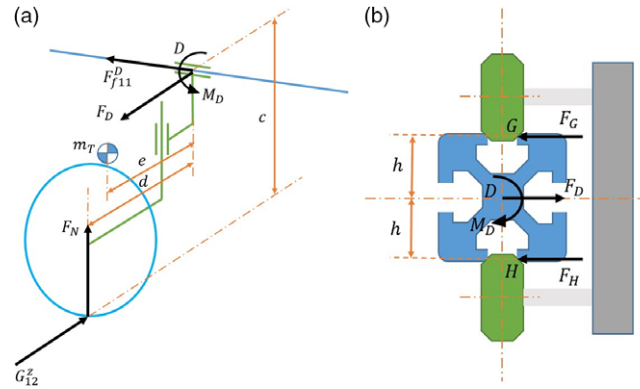
$$V_{11} = \dot{s}_{111} \tag{13}$$

Fig. 6. (a) Simplified representation of the one quarter part (b) Forces/moments acting at point D.

Consequently, the Lagrange function is rewritten as follows:

$$L = \frac{1}{2}(m_T + m_{11})\dot{s}_{111}^2 + \frac{1}{2}m_T\dot{s}_{1011}^2 + \frac{1}{2}I_3\dot{\theta}_3^2 \tag{14}$$

For no-slip condition, the relation between the angular speed of link 3 and the speed of total mass along the X-direction is determined as

$$\dot{s}_{1011} = r\dot{\theta}_3 \tag{15}$$

The total virtual work of the system is formulated in order to find generalized forces in Eq. (16). Here, $F_{ext}^E$ and $F_{ext}^F$ are the forces acting on the system along the Z-direction to move the wheel along the Z-direction in order to observe the effects of the side motion enabled by the passive rollers.

$$\delta\tilde{W} = \tilde{Q}_\theta\delta_\theta + \tilde{Q}_z\delta_z = \left(F_{ext}^E + F_{ext}^F\right)\delta_z + T_3\delta_\theta \tag{16}$$

Therefore, the column vector of generalized forces of the system is

$$Q = \begin{bmatrix} \tilde{Q}_z \\ \tilde{Q}_\theta \end{bmatrix} = \begin{bmatrix} F_{ext}^E + F_{ext}^F \\ T_3 \end{bmatrix} \tag{17}$$

There are also five dissipative forces acting on the system due to the frictional forces at the prismatic joint at points $D$, $E$ and $F$ ($F_{f11}^D$, $F_{f11}^E$, $F_{f11}^F$) and frictional forces due to the passive rollers ($G_{12}^z$) and rolling resistance force of the wheel ($F_{rol}$). These frictional forces are assumed to be the result of dry and viscous friction between the surfaces. The dry and viscous friction coefficients at points $E$ and $F$ are denoted as $\mu_{E\_dry}$ and $\mu_{F\_dry}$, and $\mu_{E\_vis}$ and $\mu_{F\_vis}$, respectively. Accordingly, frictional forces at points $E$ and $F$ and rolling resistance force are calculated as follows:

$$F_{f11}^E = [\mu_{E\_dry}sgn\,(\dot{s}_{111}) + \mu_{E\_vis}\,\dot{s}_{111}]G_{111}^{Ey} \tag{18}$$

$$F_{f11}^F = [\mu_{F\_dry}sgn\,(\dot{s}_{111}) + \mu_{F\_vis}\,\dot{s}_{111}]G_{111}^{Fy} \tag{19}$$

$$F_{rol} = \mu_{rol}m_T g \tag{20}$$

where $G_{111}^{Ey}$ and $G_{111}^{Fy}$ are normal forces acting on points $E$ and $F$ and $\mu_{rol}$ is the coefficient of rolling resistance.

The frictional force at point $D$ is affected by the abovementioned lateral frictional force. In Fig. 6, a specific direction of lateral motion is investigated. Accordingly, if the lateral motion is in the other direction, the forces and moment identified as $F_D$, $F_G$, $F_H$ and $M_D$ on Fig. 6(b) will be in the opposite
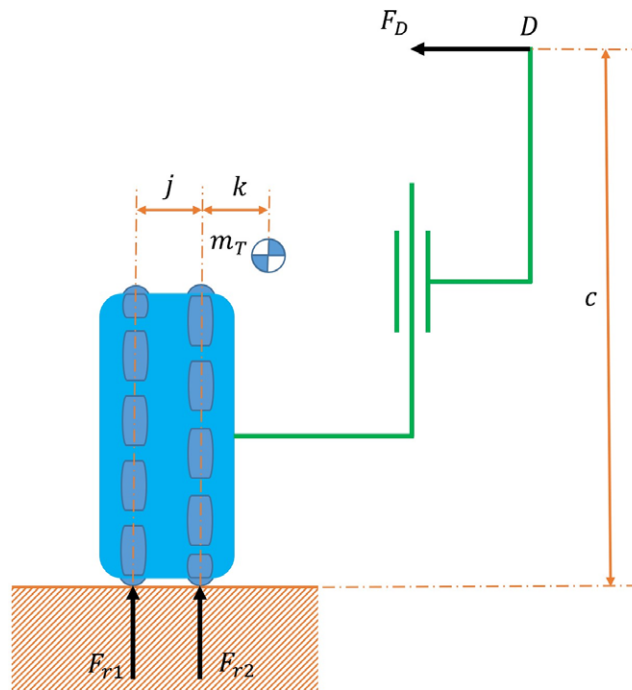
Fig. 7. Reaction forces acting on passive rollers.

directions. The frictional force at point $D$ is calculated using the dry and viscous friction coefficients denoted by $\mu_{D\_dry}$ and $\mu_{D\_vis}$ as

$$M_D = F_{Nd} - m_{Tg}\, e - G^z_{12}c \tag{21}$$

$$F_D = -G^z_{12} \tag{22}$$

$$F_H = \frac{F_{Dh} - M_D}{2h}, \quad F_G = \frac{F_{Dh} + M_D}{2h} \tag{23}$$

$$F^D_{f11} = \left[\mu_{D\_dry}sgn(\dot{s}_{1011}) + \mu_{D\_vis}\,\dot{s}_{1011}\right](|F_H| + |F_G|) \tag{24}$$

where $F_N$ is the total normal force acting on the wheel.

On the UTO wheel, there are two rows of passive rollers. During the lateral motion of the UTO wheel, the lateral frictional force is generated while these rollers roll about their own axes. Due to the lateral frictional force, the normal force on the ground applied by the rollers changes. This situation is represented in Fig. 7. Each component of the quarter model is weighed, and then this information is used in the assembly of the test setup in computer-aided design (CAD) software. The mass center location is calculated using this assembly file in CAD environment.

The reaction forces from the ground to the rollers are calculated in Eq. (25). The assumption made here is that both rollers touch the ground at all times.

$$F_{r1} = \frac{-m_{Tgk} + F_{Dc}}{j}, \quad F_{r2} = \frac{m_{Tg}(k + j) - F_{Dc}}{j} \tag{25}$$

Accordingly, the lateral frictional force on the wheel is determined from Eq. (22). Here, the dry and viscous friction coefficients between the rollers and the surface are denoted by $\mu_{R\_dry}$ and $\mu_{D\_vis}$, respectively.

$$G^z_{12} = -F_D = \left[\mu_{R\_dry}sgn\,(\dot{s}_{111}) + \mu_{R\_vis}\,\dot{s}_{111}\right](|F_{r1}| + |F_{r2}|) \tag{26}$$

Using Eqs (21) and (23), $F_D$ is calculated and substituted in Eq. (25) to calculate $F_{r1}$ and $F_{r2}$. Consequently, the normal force acting on the wheel is determined by $F_N = F_{r1} + F_{r2}$. Based on the

above mentioned equations for the Lagrange function and dissipative forces, the equations of motion are determined as presented in Eqs (27) and (28).

$$(m_T + m_{11}) \ddot{s}_{111} + G_{12}^z + F_{f11}^E + F_{f11}^F = F_{ext}^E + F_{ext}^F \tag{27}$$

$$(m_T r^2 + I_3) \ddot{\theta}_3 + (F_{f11}^D + F_{rol}) r = T_3 \tag{28}$$

Then, the equations of motion of the test setup can be written in matrix form as follows:

$$\boldsymbol{M(q)}\, \ddot{\boldsymbol{q}} + \boldsymbol{F(\dot{q})} = \boldsymbol{B(q)}\, \boldsymbol{\tau} \tag{29}$$

$$\underbrace{\begin{bmatrix} (m_T + m_{11}) & 0 \\ 0 & (m_T r^2 + I_3) \end{bmatrix}}_{\boldsymbol{M(q)}} \underbrace{\begin{bmatrix} \ddot{s}_{111} \\ \ddot{\theta}_3 \end{bmatrix}}_{\ddot{\boldsymbol{q}}} + \underbrace{\begin{bmatrix} G_{12}^z + F_{f11}^E + F_{f11}^F \\ (F_{f11}^D + F_{rol})r \end{bmatrix}}_{\boldsymbol{F(\dot{q})}} = \underbrace{\begin{bmatrix} 1 & 0 \\ 0 & 1 \end{bmatrix}}_{\boldsymbol{B(q)=I}} \underbrace{\begin{bmatrix} F_{ext}^E + F_{ext}^F \\ T_3 \end{bmatrix}}_{\boldsymbol{\tau}} \tag{30}$$

Up to now, the equations of motion are found assuming that there is no slip between the wheel and the ground. In fact, the frictional force between the wheel and the ground varies according to the amount of wheel slippage as described in the previous sections. The state of slip between the wheel and the ground can be expressed as follows:

$$\dot{s}_{1011} = r\dot{\theta}_3 \rightarrow No\ slip\ case \tag{31}$$

$$\dot{s}_{1011} \neq r\dot{\theta}_3 \rightarrow Slip\ case \tag{32}$$

For slip case, Eq. (28) becomes

$$m_T \ddot{s}_{1011} r + I_3 \ddot{\theta}_3 + (F_{f11}^D + F_{rol}) r = T_3 \tag{33}$$

The traction force, $F_{trac}$, applied to the vehicle is calculated as follows:

$$F_{trac} = m_T \ddot{s}_{1011} + (F_{f11}^D + F_{rol}) \tag{34}$$

This force is related to the frictional force between the wheel and the ground. Traction force can be also estimated with the LuGre model whose formulation is given in the previous section in Eq. (4). Then, the longitudinal dynamic model is represented with the following four state variables:

$$x_1 = \dot{s}_{1011} \tag{35}$$

$$x_2 = \dot{\theta}_3 \tag{36}$$

$$x_3 = p \tag{37}$$

$$x_4 = \dot{s}_{111} \tag{38}$$

Equations (4) and (5) can be rewritten using these states defined above as follows:

$$V_r = x_2 r - x_1 \tag{39}$$

$$\dot{x}_3 = (x_2 r - x_1) - \frac{\sigma_0 |x_2 r - x_1|}{g(x_2 r - x_1)} x_3 \tag{40}$$

$$F_{trac} = F_N \left[ \sigma_0 x_3 + \sigma_1 \left[ (x_2 r - x_1) - \frac{\sigma_0 |x_2 r - x_1|}{g(x_2 r - x_1)} x_3 \right] + \sigma_2 (x_2 r - x_1) \right] \tag{41}$$

$$F_{trac} = F_N \left[ \sigma_0 x_3 \left[ 1 - \frac{\sigma_1 |x_2 r - x_1|}{g(x_2 r - x_1)} \right] + (x_2 r - x_1) [\sigma_1 + \sigma_2] \right] \tag{42}$$
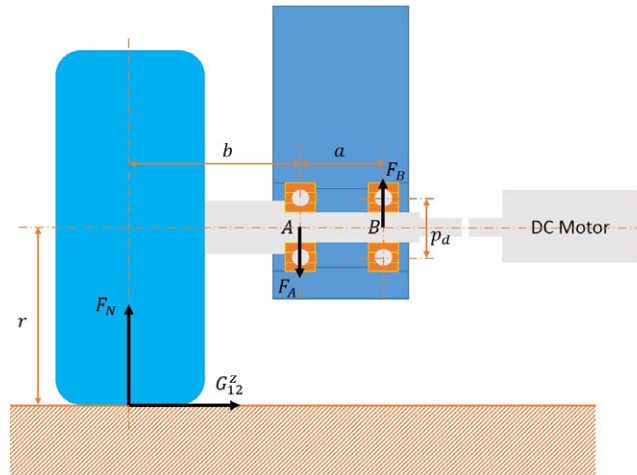
Fig. 8. Reaction forces acting on the bearings of the wheel shaft.

Also, the first two state equations based on Eqs (33) and (34) are written as

$$\dot{x}_1 = \frac{1}{m_T} \left[ F_{trac} - \left( F_{f11}^D + F_{rol} \right) \right] \tag{43}$$

$$\dot{x}_2 = \frac{1}{I_3} \left[ T_3 - r F_{trac} \right] \tag{44}$$

In the test setup, torque $T_3$ is generated by a DC motor. The torque generated by a DC motor is related to armature current, $i$, and motor's torque constant, $K_t$.

$$T_m = K_t i \tag{45}$$

The torque value applied by the output shaft of the motor is calculated as:

$$T_{m\_shaft} = K_t i - T_{nl} - J_r \frac{d\omega}{dt} \tag{46}$$

where $T_{nl}$ is no load friction torque of the motor shaft, $J_r$ is motor's rotor moment of inertia calculated about its rotation axis, and $\frac{d\omega}{dt}$ is the angular acceleration of the motor shaft. The output torque of the gearbox, $T_{gear\_shaft}$, is formulated as follows:

$$T_{gear\_shaft} = \left( T_{m\_shaft} - J_g \frac{d\omega}{dt} \right) E G_r \tag{47}$$

where $E$ is the efficiency of the gearbox, $G_r$ is the torque amplification ratio (inverse of the speed reduction ratio) of the gear, and $J_g$ is the moment of inertia of the gears lumped to the input shaft of the gear.

The normal forces acting on the bearings change due to the lateral motion of the wheel, which is represented in Fig. 8.

The total friction torque acting on the bearings is calculated by determining the normal forces acting on the bearings ($F_A$ and $F_B$).

$$F_A = \frac{F_N(a + b) - G_{12}^z r}{a}, \quad F_B = \frac{F_N b - G_{12}^z r}{a} \tag{48}$$

$$T_{friction} = \left[ \mu_{bearing\_dry} sign(x_2) + \mu_{bearing\_vis} \, x_2 \right] \left( |F_A| + |F_B| \right) \left( \frac{p_d}{2} \right) \tag{49}$$

where $\mu_{bearing\_dry}$ and $\mu_{bearing\_vis}$ are the dry and viscous friction coefficients of the bearing and $p_d$ is the pitch diameter of bearing. The effective applied torque on the wheel is calculated as:

$$T_3 = T_{gear\_shaft} - T_{friction} \tag{50}$$

Consequently, Eq. (44) is rewritten as follows:

$$\dot{x}_2 = \frac{1}{I_3 + \left(J_r + J_g\right) EG_r{}^2} \left[ \left(K_t i - T_{nl}\right) EG_r - T_{friction} - rF_{trac} \right] \tag{51}$$

## 3. Parameter identification

### 3.1. Test procedure

Parameter identification tests are carried out on three different floor types. The surfaces where these tests are carried out are natural stone, PVC floor covering and paperboard surface placed on the floor. To identify the LuGre wheel friction model parameters for these floor types, the relation between the relative speed and the traction force must be measured. Tests are carried out by supplying 24 V DC and different levels of constant current to the DC motor that actuates UTO wheel. In the first test, the current value supplied to the motor is set to a constant 0.15 A. A larger constant current is used for the next tests and is raised up to the maximum constant current of 1.5 A. The traction force corresponding to each test is calculated by applying Eq. (34). The total mass of the one-quarter part of the test setup and the frictional force of the linear guide are measured to be $m_T = 3.9593$ kg and 0.304 N, respectively. The identification test procedure is set for each floor type as follows:

(1) Supply the selected constant current to the DC motor mounted to the UTO wheel within the predefined working range.
(2) Calculate the speed of the one-quarter model using the measurements from the encoders at the rear side of the DC motor.
(3) Calculate the speed of the one-quarter model (actual speed) using the measurements from the encoders located on the measurement wheel moving on the linear guide.
(4) Calculate the relative speed by the difference between the two calculations of one-quarter model's speed.
(5) Measure acceleration of the one-quarter model with an accelerometer mounted on it.
(6) Compute the traction force by applying Eq. (34) and using the measured acceleration at step 5.
(7) Move the one-quarter model back to the starting position, set the constant current value to an increased value and repeat the test.
(8) After the tests are completed, supply the measured relative speed data for each test to the LuGre model as inputs and calculate the corresponding traction forces.
(9) Identify the optimal model parameters that satisfy each test traction force result and LuGre model traction force outputs.

The whole test procedure is represented in Fig. 9.

### 3.2. Parameter identification and model validation tests

The Humusoft data acquisition card (DAQ) is used for data acquisition with a sampling frequency of 1 kHz during identification and validation tests. The calculated speeds of the one-quarter model from the encoder data received from the linear guide ($\dot{s}_{1011}$) and from the encoder attached to the rear end of the motor driving the UTO wheel ($r\dot{\theta}_3$) (UTO wheel speed), during one of the tests on natural stone floor carried out with 1.35 A constant current, are represented in Fig. 10.

As can be observed in Fig. 10, when the constant current is applied to the motor that actuates the UTO wheel, the one-quarter model accelerates until the motor reaches the maximum speed. After the motor reaches the maximum speed at 0.7 s of the test, the one-quarter model continues the motion at this constant maximum speed until a safe location after which the one-quarter model can come to a full stop within the test setup's workspace. While the speed calculated from the UTO wheel is larger than the actual speed of the one-quarter model during the acceleration regime of the motion, these values are close to each other during the constant speed portion of the motion. The relative speed that shows the difference between the speed calculated from the UTO wheel and the actual speed of the one-quarter model during experiments on different floor types are presented in Fig. 11.

After collecting data for each test with different constant current values, the parameters of the LuGre wheel friction model that produce the most similar results for each test's traction forces are
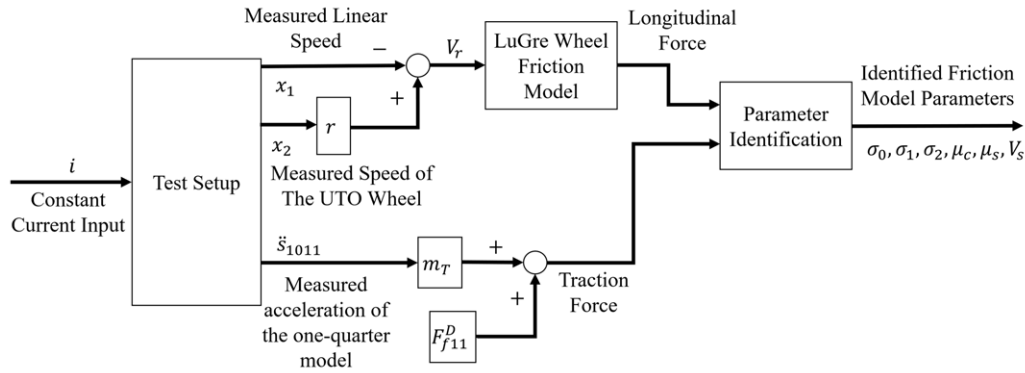
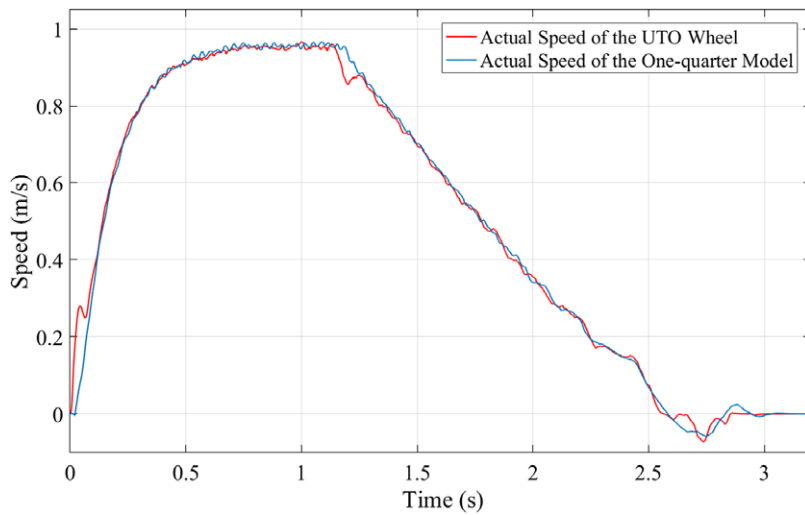Fig. 9. Procedure of parameter identification test.



Fig. 10. Calculated speed of the one-quarter model from the UTO wheel and the actual speed during the test on natural stone floor carried out with 1.35 A constant current.
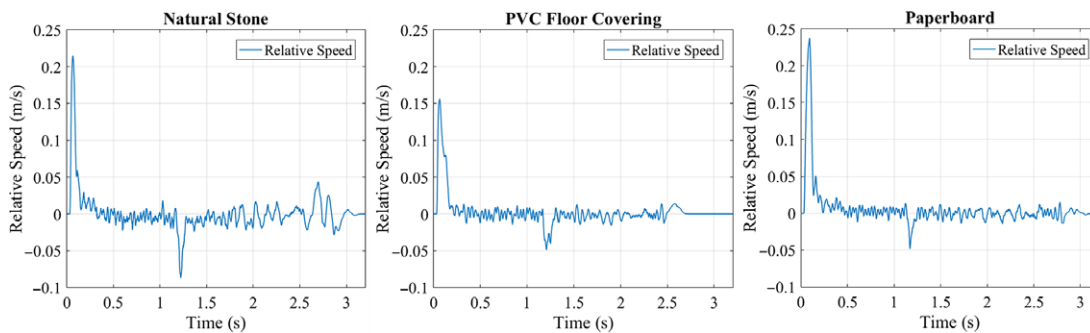


Fig. 11. Relative speed during the tests on three floor types carried out with 1.35 A.

identified. In this identification routine, the measured relative speed values are given as the input in the constructed Matlab™ Simulink™ model, and then the estimated traction forces, which are the output of the LuGre model, are compared with the actual traction forces. The Matlab™ parameter estimation toolbox is used during this identification of the LuGre model parameters. The identified LuGre friction model parameters for three floor types are presented in Table I. The measured and the estimated traction force values with the identified parameters for 1.35 A constant current are shown in Fig. 12.

Table I. Identified LuGre friction model parameters.

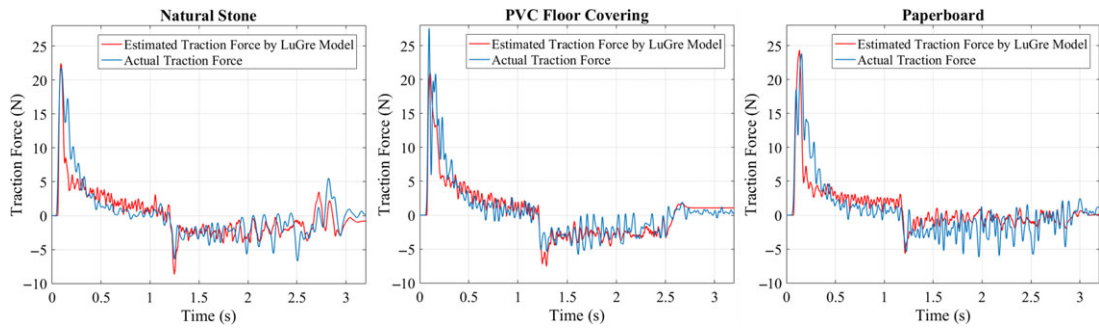| Floor type | Parameters | | | | | |
|---|---|---|---|---|---|---|
| | $V_s(m/s)$ | $\mu_c$ | $\mu_s$ | $\sigma_0(m^{-1})$ | $\sigma_1(s/m)$ | $\sigma_2(s/m)$ |
| Natural stone | 1.9643 | 0.12 | 0.1205 | 11.451 | 0.0809 | 2.4490 |
| PVC floor covering | 0.0044 | 0.12 | 0.15 | 49.933 | 0.3720 | 2.8084 |
| Paperboard | 0.8170 | 0.04 | 0.07 | 54.724 | 0.6146 | 2.4028 |



Fig. 12. Estimated and actual traction forces during the tests with 1.35 A.
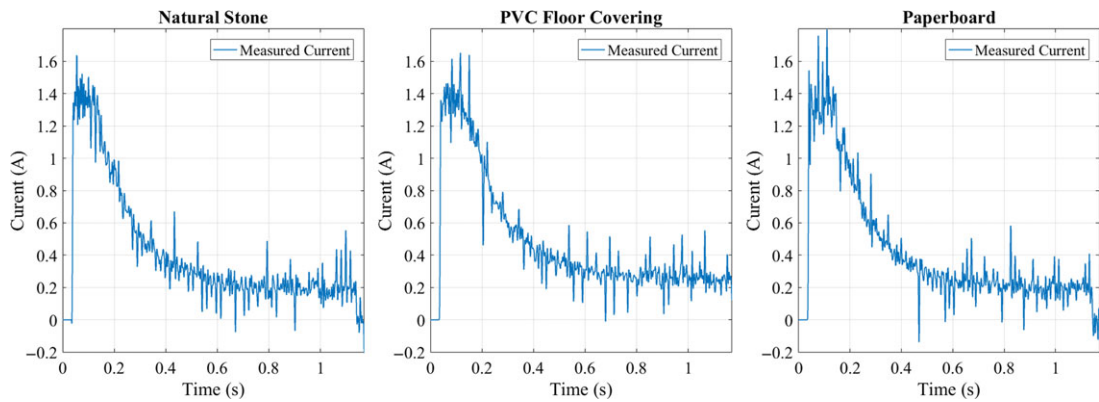


Fig. 13. Measured current on the output monitor of the motor driver during validation tests with a constant current of 1.35 A.
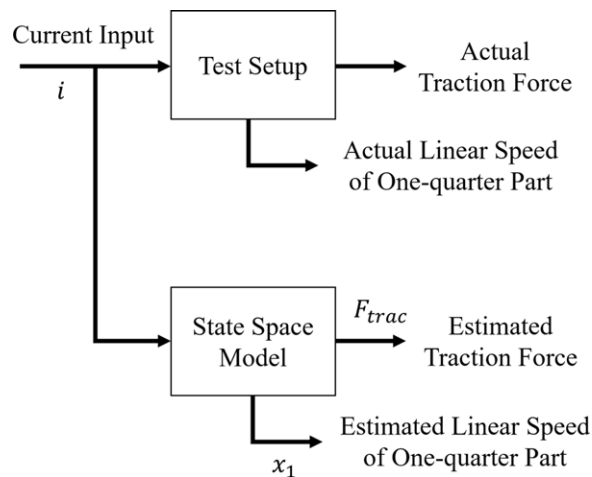


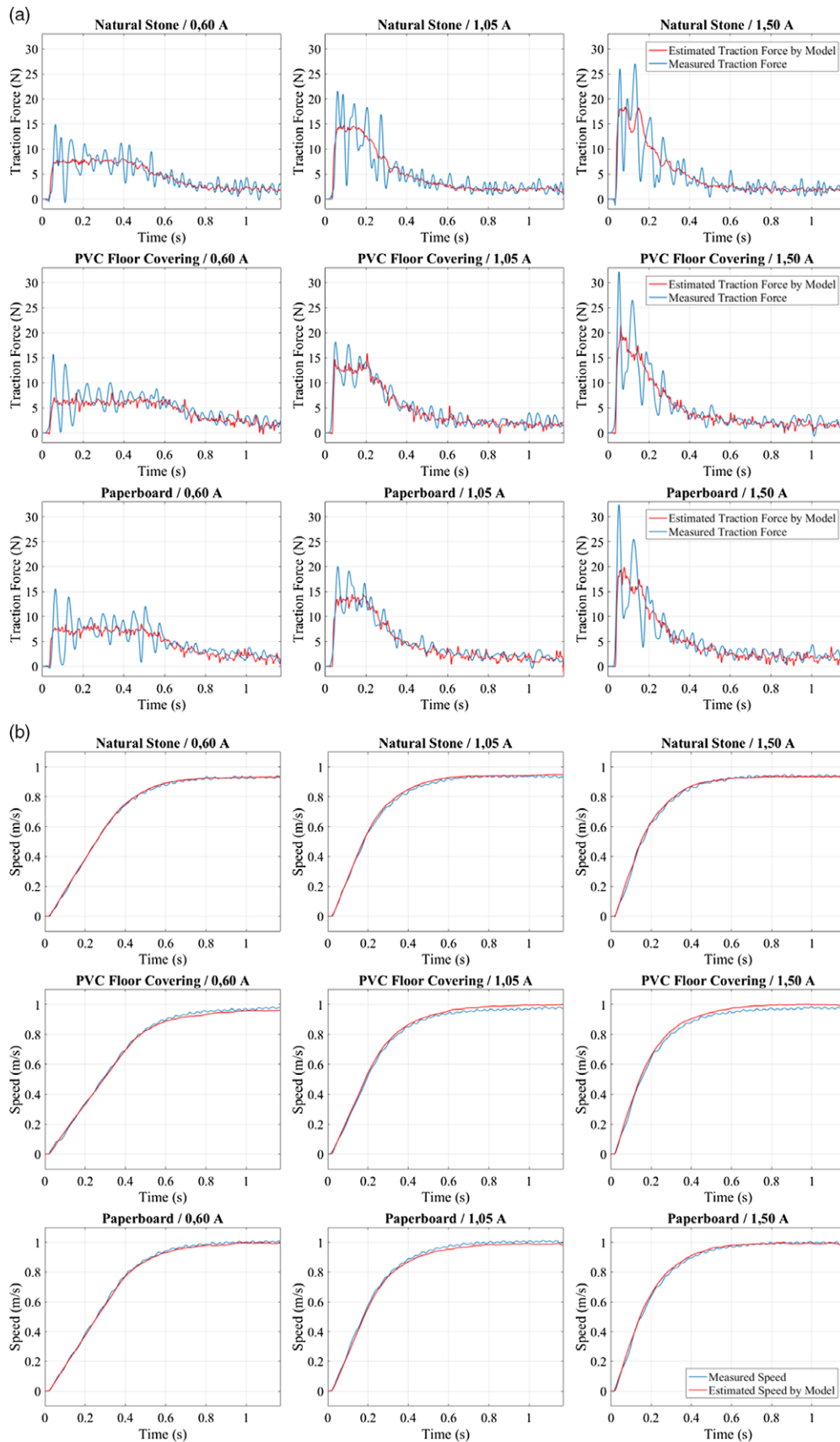Fig. 14. Model validation test procedure.

Fig. 15. Model validation test results. (a) Comparison between measured and estimated traction forces. (b) Comparison between estimated and actual linear speeds of the one-quarter model.

Table II. RMS values of errors between measured and estimated speeds of the one-quarter model for each test.

| Mass of the one-quarter model (kg) | Current input (A) | Floor types | | |
| | | Natural stone | PVC floor covering | Paperboard |
| | | RMS values of error (m/s) | | |
| 3.9593 | 0.45 | 0.024 | 0.037 | 0.035 |
| | 0.60 | 0.016 | 0.035 | 0.006 |
| | 0.75 | 0.007 | 0.014 | 0.010 |
| | 0.90 | 0.010 | 0.008 | 0.021 |
| | 1.05 | 0.012 | 0.019 | 0.017 |
| | 1.20 | 0.016 | 0.009 | 0.011 |
| | 1.35 | 0.020 | 0.017 | 0.021 |
| | 1.50 | 0.012 | 0.024 | 0.013 |
| 2.9593 | 0.45 | 0.022 | 0.036 | 0.031 |
| | 0.60 | 0.015 | 0.013 | 0.012 |
| | 0.75 | 0.013 | 0.011 | 0.011 |
| | 0.90 | 0.008 | 0.010 | 0.008 |
| | 1.05 | 0.022 | 0.011 | 0.015 |
| | 1.20 | 0.016 | 0.010 | 0.014 |
| | 1.35 | 0.025 | 0.014 | 0.012 |
| | 1.50 | 0.029 | 0.015 | 0.025 |
| 1.9593 | 0.45 | 0.035 | 0.019 | 0.022 |
| | 0.60 | 0.015 | 0.016 | 0.022 |
| | 0.75 | 0.029 | 0.016 | 0.019 |
| | 0.90 | 0.018 | 0.018 | 0.022 |
| | 1.05 | 0.028 | 0.026 | 0.025 |
| | 1.20 | 0.038 | 0.033 | 0.025 |
| | 1.35 | 0.037 | 0.031 | 0.032 |
| | 1.50 | 0.025 | 0.029 | 0.015 |

After identifying the model parameters, the validation procedure of the longitudinal system dynamics given in Section 2 is carried out. In the validation tests, the motor is driven with a constant current value from starting position until the safe position from which the system can come to a full stop within the limits of the workspace. During the total motion, the actual current value is measured via the motor driver's current monitor output port. Throughout the test, the constant current value is set to 1.35 A. As can be observed in Fig. 13, the current value is the constant 1.35 A, while the one-quarter model is in acceleration regime. After the one-quarter model reaches the maximum speed, the current supplied to the motor slowly decreases until a constant current value. This constant current value produces the necessary amount of torque to compensate for the frictional force at the linear guide and no-load torque value of the motor, which is due to the motor's internal friction and armature resistance and rolling resistance of the wheel. As can be seen in Fig. 13, when the measured current value is about 0.2 A at a constant speed part of the motion for natural stone and paperboard floor types, this value is larger than 0.2 A for PVC floor covering due to higher rolling resistance.

These measured current values for each test are supplied as inputs to the model with the identified parameters, whose equations are given in Section 2.2, and the estimated traction forces and speed of the one-quarter model for each test data are the outputs of the state space model (Fig. 14). These estimated traction forces and speed of the one-quarter model are compared with the measured actual values. These comparisons for each test with different constant current values are presented in Fig. 15(a) and 15(b) for traction forces and speeds, respectively. In addition, the tests are repeated with changing the weight of the one-quarter model of the mobile robot and the estimated and measured speed values are compared. Root mean square (RMS) values of the errors between measured and estimated speeds of the one-quarter model for each test result are presented in Table II.
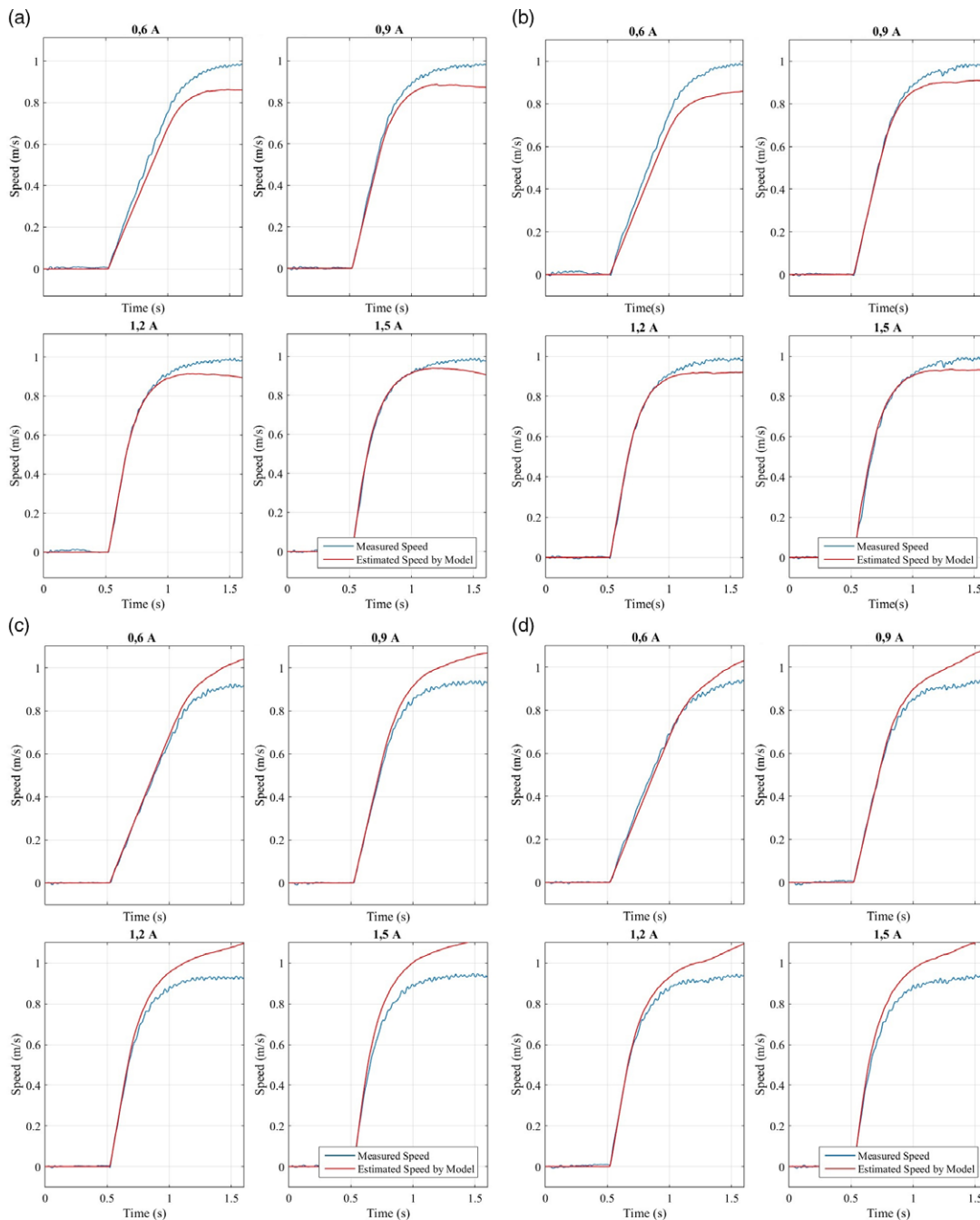
Fig. 16. Test results for zero lateral frictional force: (a) 0.35 m/s lateral speed, (b) 0.50 m/s lateral speed, (c) –0.35 m/s lateral speed, (d) –0.50 m/s lateral speed.

## 4. Effect of lateral frictional force on the longitudinal motion of the one-quarter of the mobile robot

In this part of the study, the effect of lateral frictional force of the wheel on the longitudinal motion of the one-quarter of the mobile robot is investigated. The longitudinal motion of the one-quarter of the robot in the test setup is influenced by various frictional forces. Although the lateral frictional forces of the UTO wheels are very small compared to the conventional wheels, ignoring the friction in lateral direction degrades the accuracy of the longitudinal model. In order to observe this situation, tests are carried out at different lateral speeds with the test setup on the natural stone floor. To observe the effect of lateral motion, while the one-quarter model is in the initial position, the constant lateral

Table III. RMS values of errors between measured and estimated speeds of the one-quarter model for each test achieved with zero lateral frictional force assumption.

| Lateral motion at positive direction | | | |
|---|---|---|---|
| **0.6 A** | **0.9 A** | **1.2 A** | **1.5 A** |
| 0.2 m/s | 0.045 | 0.029 | 0.033 | 0.024 |
| 0.35 m/s | 0.068 | 0.054 | 0.040 | 0.027 |
| 0.5 m/s | 0.075 | 0.038 | 0.033 | 0.029 |
| 0.65 m/s | 0.072 | 0.040 | 0.028 | 0.033 |

| Lateral motion in negative direction | | | |
|---|---|---|---|
| **0.6 A** | **0.9 A** | **1.2 A** | **1.5 A** |
| –0.2 m/s | 0.023 | 0.055 | 0.051 | 0.078 |
| –0.35 m/s | 0.047 | 0.066 | 0.079 | 0.102 |
| –0.5 m/s | 0.034 | 0.064 | 0.067 | 0.093 |
| –0.65 m/s | 0.057 | 0.082 | 0.088 | 0.103 |

Table IV. RMS values of errors between measured and estimated speeds of the one-quarter model for each test achieved with considering effect of the lateral frictional force in the model.

| Lateral motion in positive direction | | | |
|---|---|---|---|
| **0.6 A** | **0.9 A** | **1.2 A** | **1.5 A** |
| 0.2 m/s | 0.021 | 0.005 | 0.008 | 0.009 |
| 0.35 m/s | 0.029 | 0.013 | 0.011 | 0.024 |
| 0.5 m/s | 0.029 | 0.014 | 0.022 | 0.032 |
| 0.65 m/s | 0.024 | 0.019 | 0.029 | 0.028 |

| Lateral motion in negative direction | | | |
|---|---|---|---|
| 0.6 A | 0.9 A | 1.2 A | 1.5 A |
| –0.2 m/s | 0.018 | 0.018 | 0.015 | 0.041 |
| –0.35 m/s | 0.016 | 0.008 | 0.020 | 0.044 |
| –0.5 m/s | 0.059 | 0.023 | 0.019 | 0.018 |
| –0.65 m/s | 0.047 | 0.018 | 0.014 | 0.024 |

speed demand is given to the linear guide. As soon as the linear guide reaches a constant lateral speed, the one-quarter model is driven with constant current from the initial position to the safe position. The test is repeated with various lateral speed and current values.

Initially, the lateral frictional force is assumed to be zero in the model and the actual speed of the one-quarter model is compared with the estimated speed. Test results achieved with different lateral speeds are represented in Fig. 16. The RMS values of the error between the actual and estimated longitudinal speed of the one-quarter of the robot for tests achieved with different lateral speeds are given in Table III.

As a next step, the effect of lateral frictional force caused by the lateral motion is considered in the model. The same test results analyzed against the no lateral friction model are used in this analysis. The results with the lateral friction model are represented in Fig. 17. The RMS values of the errors between the actual and estimated speed values obtained as a result of this analysis with the lateral friction model are given in Table IV.
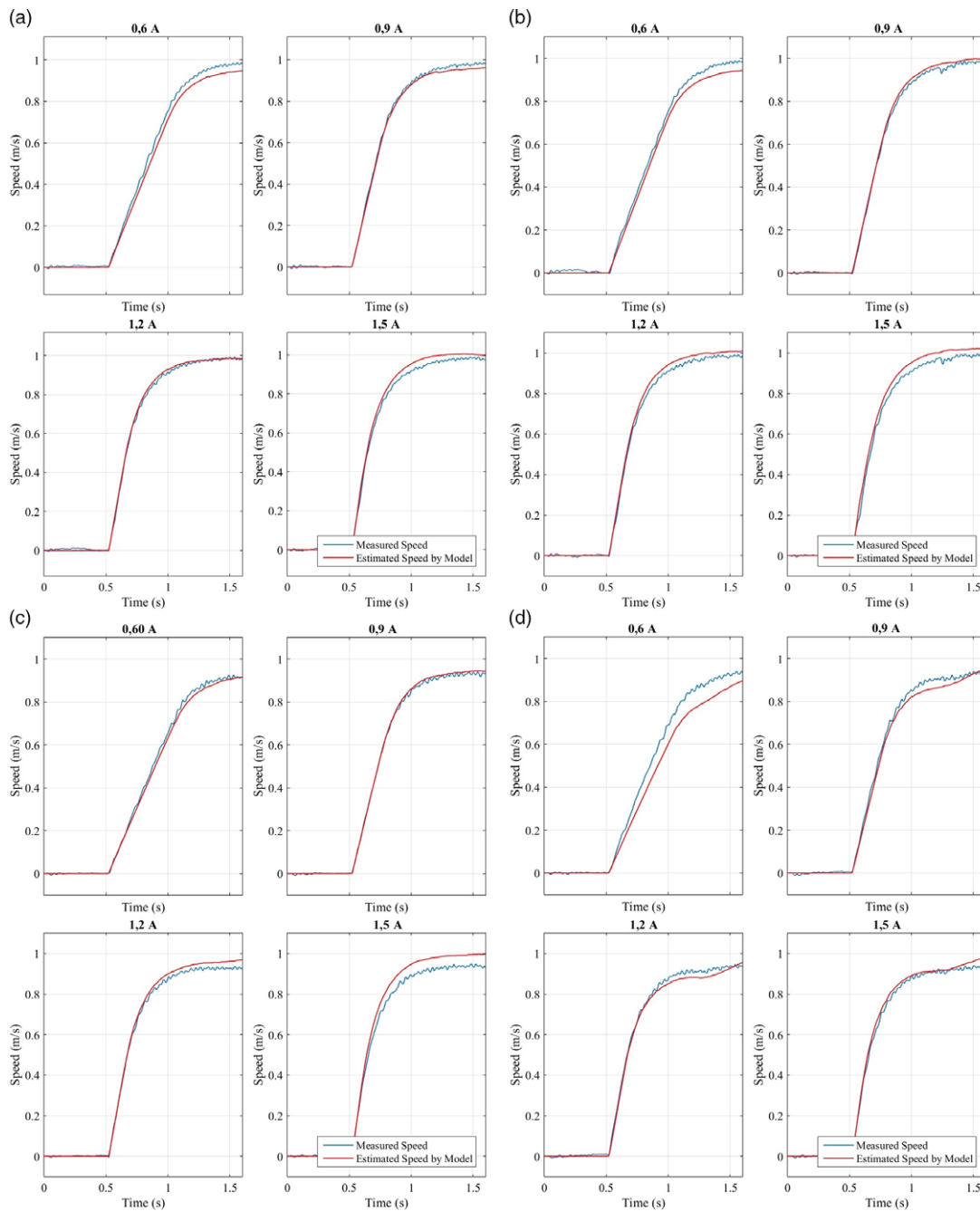
Fig. 17. Test results for considering the lateral frictional force in the model: (a) 0.35 m/s lateral speed, (b) 0.50 m/s lateral speed, (c) –0.35 m/s lateral speed, (d) –0.50 m/s lateral speed.

## 5. Conclusion

The friction characteristic between the wheel and the ground is an important part of vehicle dynamics studies, which is also important for improving the control of mobile robots. In this study, the longitudinal friction characteristic of a UTO wheel is studied via implementing the LuGre friction model. As a result of the tests, the LuGre model parameters are identified for the omnidirectional wheel and three different floor types. Also, full-system model validation tests with the identified wheel friction model parameters are carried out in which the measured traction forces and the actual speeds of the one-quarter model are compared with the estimated speeds and traction forces.

During validation tests, the current inputs to the motor coupled to the UTO are obtained via the driver of the motor. Consequently, the output signals received from the model are noisy due to the

use of these actual currents as input signals. Relatively higher-magnitude oscillations are observed in the measured results of the traction forces due to vibrations during the motion of this specially structured UTO. The main reason for this vibration is the transition of contact from one free roller on the UTO wheel to the next free roller. Irrespective of these oscillations, when the plots in Fig. 15(a) are investigated, it can be concluded that the estimated traction forces closely match the measured ones. Additionally, the measured speed of the one-quarter model is compared with the speed output received from the model. The difference between them is considerably low, which means that a reliable model for the one-quarter model with the UTO wheel is obtained. Therefore, the obtained friction model can be used in the future for traction control and odometry studies.

Omnidirectional wheels have passive rollers that allow motion in the parallel direction to the rotation axis of the wheel, which significantly reduces the lateral frictional force. However, this frictional force must still be considered in the vehicle model. In the literature, the effect of lateral frictional force in the dynamic equations of such robots is considered only in two-dimensional space as the robot moves on the plane. However, when the effect of the lateral frictional force is examined from a three-dimensional perspective, this force changes the reaction forces and moments on the various rotating and moving elements. Ignoring the effect of lateral frictional force on these elements causes inaccuracies in the friction model of the robot. In the last part of the study, the effect of lateral frictional force on the motion of the robot is investigated. According to the test results, when the lateral frictional force is ignored in the model, it was observed that the estimated speed of the model did not match with the measured speed, and the error between the estimated speed and actual speed increased drastically. However, when the lateral friction was considered in the longitudinal model, the error in speed estimation was considerably reduced.

The UTO wheels used in mobile robots have single-row or double-row rollers, which is the one used in this work. It is not possible to talk about a continuous friction characteristic on the longitudinal axis due to the spaced structure of the rollers in UTO wheels using single-row rollers. Therefore, it is not possible to model longitudinal friction in UTO wheels that have single-row rollers. The urethane material, which is used in the UTO wheel in the study, or rubber, which has very close friction characteristics, can be used in the rollers of UTO wheels suitable for use in mobile robots. These two materials are also used in many robot wheels. Another factor that specifies the friction between the wheel and the ground is the type of ground. The identified parameters of the LuGre friction model for three different floor types can be used for modeling the friction between a mobile robot wheel using the same material and ground types that are similar in structure with this study. In order to model the friction between mobile robot wheels using different types of materials and ground types that have different structures, the model parameters must be identified with the procedure described in Section 3.

In traction control systems used in wheeled terrestrial vehicles, it is aimed to estimate the amount of slippage between the wheel and the ground and to reduce the speed of the slipped wheel to ensure holding onto the ground. Thanks to the model obtained as the output of the study, wheel slippage can be estimated for usual cases. In the case of an unusual slippage on one of the wheels in the mobile robot, the estimated value differs from the actual value. In this way, a control algorithm similar to the traction control systems used in terrestrial vehicles can be applied in mobile robots by determining the unusual wheel slippage.

## References

1. K. Tadakuma and R. Tadakuma, "Mechanical Design of "Omni-Ball": Spherical Wheel for Holonomic Omnidirectional Motion," In: Proceedings of the 3rd Annual IEEE Conference on Automation Science and Engineering (2007) pp. 788–794.
2. K.-L. Han, A.-K. Choi, J. Kim, H. Kim and J. S. Lee, "Design and Control of Mobile Robot with Mecanum Wheel," In: ICROS-SICE International Joint Conference (2009) pp. 2932–2937.
3. S. Ishida and H. Miyamoto, "Ball Wheel Drive Mechanism for Holonomic Omnidirectional Vehicle," *In: World Automation Congress* (2010).
4. M. A. Al Mamun, M. T. Nasir and A. Khayyat, "Embedded system for motion control of an omnidirectional mobile robot," *IEEE Access* **6**, 6722–6739 (2018).
5. Z. Li, C. Yang, C.-Y. Su, J. Deng and W. Zhang, "Vision-based model predictive control for steering of a nonholonomic mobile robot," *IEEE Trans Control Syst Technol.* **24**(2), 553–564 (2016).
6. R. Oftadeh, M. M. Aref, R. Ghabcheloo and J. Mattila, "Mechatronic design of a four-wheel steering mobile robot with fault-tolerant odometry feedback," In: 6th IFAC Symposium on Mechatronic Systems (2013) pp. 663–669.

7. J. Yi, H. Wang, J. Zhang, D. Song, S. Jayasuriya and J. Liu, "Kinematic modeling and analysis of skid-steered mobile robots with applications to low-cost inertial-measurement-unit-based motion estimation," *IEEE Trans Robot.* **25**(5), 1087–1097 (2009).

8. Y. Tian and N. Sarkar, "Control of a mobile robot subject to wheel slip," *J Intell Robot Syst.* **74**(3–4), 915–929 (2014).

9. L. Jetto, S. Longhi and D. Vitali, "Localization of a wheeled mobile robot by sensor data fusion based on a fuzzy logic adapted kalman filter," In: IFAC Intelligent Autonomous Vehicles (1998), pp. 213–218.

10. N. Ganganath and H. Leung, "Mobile robot localization using odometry and kinect sensor," **In**: *IEEE International Conference on Emerging Signal Processing Applications* (2012), pp. 91–94.

11. L. Marin, M. Valles, A. Soriano, A. Valera and P. Albertos, "Event-based localization in Ackermann steering limited resource mobile robots," *IEEE/ASME Trans Mech.* **19**(4), 1171–1182 (2014).

12. H. Peela, S. Luo, A. G. Cohn and R. Fuentes, "Localisation of a mobile robot for bridge bearing inspection," *Autom Constr.* **94**, 244–256 (2018).

13. K. Iagnemma and C. C. Ward, "Classification-based wheel slip detection and detector fusion for mobile robots on outdoor terrain," *Autonomous Robot.* **26**(1), 33–46 (2009).

14. G. Erdogan, L. Alexander and R. Rajamani, "Estimation of tire-road friction coefficient using a novel wireless piezoelectric tire sensor," *IEEE Sens J.* **11**(2), 267–279 (2011).

15. J. J. Rath, K. C. Veluvolu and M. Defoort, "Simultaneous estimation of road profile and tire road friction for automotive vehicle," *IEEE Trans Veh Technol.* **64**(10), 4461–4471 (2015).

16. A. K. Madhusudhanan, M. Corno, M. A. Arat and E. Holweg, "Load sensing bearing based road-tyre friction estimation considering combined tyre slip," *Mechatronics* **39**, 136–146 (2016).

17. Y.-H. Liu, T. Li, Y.-Y. Yang, X.-W. Ji and J. Wu, "Estimation of tire-road friction coefficient based on combined APF-IEKF and iteration algorithm," *Mech Syst Signal Process.* **88**, 25–35 (2017).

18. L. Li, F.-Y. Wang and Q. Zhou, "Integrated longitudinal and lateral tire/road friction modeling and monitoring for vehicle motion control," *IEEE Trans Intell Transp Syst.* **7**(1), 1–19 (2006).

19. R. Balakrishna and A. Ghosal, "Modeling of slip for wheeled mobile robots," *lEEE Trans Robot Autom.* **11**(1), 126–132 (1995).

20. R. L. Williams, B. E. Carter, P. Gallina and G. Rosati, "Dynamic model with slip for wheeled omnidirectional robots," *IEEE Trans Robot Autom.* **18**(3), 285–293 (2002).

21. J. Y. Wong, Theory of Ground Vehicles (John Wiley & Sons, NY, USA, 3rd Edition, 2001).

22. R. Rajamani, Vehicle Dynamics and Control (Springer, NY, USA, 2006).

23. H. Pacejka, Tire and Vehicle Dynamics (Butterworth-Heinemann, Oxford, UK, 3rd Edition, 2012).

24. C. Canudas-de-Wit, P. Tsiotras, E. Velenis, M. Basset and G. Gissinger, "Dynamic friction models for road/tire longitudinal interaction," *Vehicle System Dynamics* **39**, 189–226 (2003).

25. C. L. Clover and J. E. Bernard, "Longitudinal tire dynamics," *Veh Syst Dyn.* **29**, 231–259 (1998).

26. P. R. Dahl, "A solid friction model," The Aerospace Corporation (1968).

27. C. Canudas-de-Wit and P. Tsiotras, "Dynamic tire friction models for vehicle traction control," **In**: *Proceedings of the 38th IEEE Conference on Decision and Control* (1999) pp. 3746–3751.